Matter

CellPress

Article

Thermally induced structural evolution and nanoscale interfacial dynamics in Bi-Sb-Te layered nanostructures

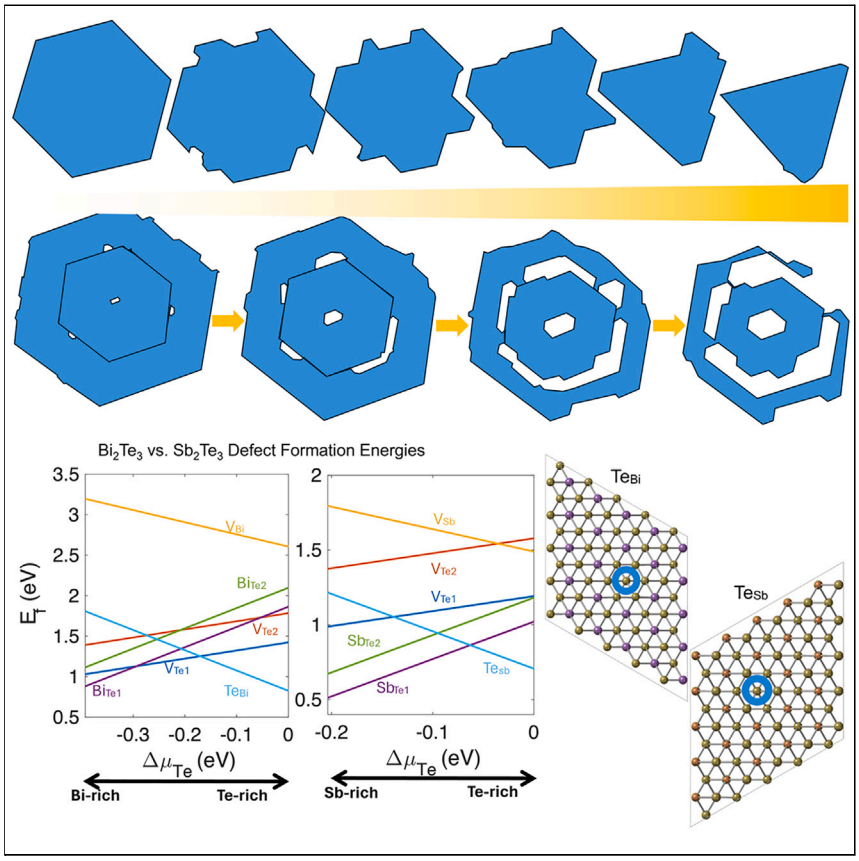

We directly visualize how defects and interfaces drive anisotropic sublimation pathways at the nanoscale using advanced microscopy coupled with theoretical calculations. Understanding these structural dynamics is crucial for designing robust low-dimensional topological insulators for applications like energy storage and energy-efficient electronics. Furthermore, the findings outline potential routes to thermally introduce defects and engineer deliberate nanoporous structures, enabling new functionalities like enhanced biosensing and gas separation.

3 Understanding
Dependency and conditional studies on material behavior

Parivash Moradifar, Tao Wang, Nadire Nayir, ..., Pulickel Ajayan, Adri C.T. van Duin, Nasim Alem

pmoradi@stanford.edu (P.M.)
nua10@psu.edu (N.A.)

Highlights

Directly visualized nanoscale dynamics and sublimation pathways in Bi-Sb-Te systems

Revealed how structural heterogeneities drive anisotropic sublimation processes

Identified role of defects, edge types, and formation energies in sublimation processes

Established a multimodal framework extendable to other vdW metal chalcogenide systems

Moradifar et al., Matter 7, 1–16
October 2, 2024
https://doi.org/10.1016/j.matt.2024.08.006

Please cite this article in press as: Moradifar et al., Thermally induced structural evolution and nanoscale interfacial dynamics in Bi-Sb-Te layered nanostructures, Matter (2024), https://doi.org/10.1016/j.matt.2024.08.006

Matter

CellPress

Article

Thermally induced structural evolution and nanoscale interfacial dynamics in Bi-Sb-Te layered nanostructures

Parivash Moradifar,[1,2,8,*] Tao Wang,[3,4] Nadire Nayir,[3,4,5] Tiva Sharifi,[6,7] Ke Wang,[1] Pulickel Ajayan,[6] Adri C.T. van Duin,[3,4] and Nasim Alem[1,*]

SUMMARY

Layered chalcogenides, including Bi-Sb-Te ternary alloys and heterostructures, are renowned as thermoelectric and topological insulators and have recently been highlighted as plasmonic building blocks beyond noble metals. We conduct joint *in situ* transmission electron microscopy and density functional theory calculations to investigate the temperature-dependent nanoscale dynamics and interfacial properties, identifying the role of native defects and edge configurations in the anisotropic sublimation of Bi_2Te_3-Sb_2Te_3 heterostructures and $Sb_{2-x}Bi_xTe_3$ alloys. We report structural dynamics, including edge evolution, layer-by-layer sublimation, and the formation and coalescence of thermally induced polygonal nanopores. These nanopores are initiated by preferential dissociation of tellurium, reducing thermal stability in heterostructures. Triangular and quasi-hexagonal configurations dominate nanopore structures in heterostructures. Our calculations reveal antisite defects (Te_{Sb} and Te_{Bi}) as key players in defect-assisted sublimation. These findings enhance our understanding of nanoscale dynamics and assist in designing tunable low-dimensional chalcogenides.

INTRODUCTION

V-VI-group chalcogenides such as bismuth telluride (Bi_2Te_3) and antimony telluride (Sb_2Te_3) are known for their outstanding thermoelectric (TE) and topological insulator (TI) properties.[1] Exhibiting gapless metallic surface states, they have garnered significant attention in the field of nanophotonics[2,3] and have also been proposed as new emerging plasmonic building blocks beyond noble metals (Ag and Au).[4,5] In particular, providing multiple edges, large surface areas, and strong light-matter interaction in comparison with their bulk counterparts, they are particularly advantageous for plasmonic applications[6] and optical switching, and as catalysts for energy conversion applications.[3,7]

To unlock the full potential of low-dimensional chalcogenides, it is imperative to design tunable platforms at the atomic level and to be able to manipulate the structure with atomic precision. This is because local microstructural heterogeneities (i.e., vacancies, antisites, dopants, interfaces, and edges) can significantly alter the macroscopic properties. Therefore, understanding and controlling the atomic structure is the key to ultimately designing tunable low-dimensional material systems. Microstructural heterogeneities can be considered as intrinsic (pre-existing) or extrinsic (externally induced) defects. While intrinsic defects naturally exist in the

PROGRESS AND POTENTIAL

This work represents advances in understanding the nanoscale dynamics and sublimation pathways in Bi-Sb-Te ternary metal chalcogenides. By combining direct visualization from *in situ* TEM with atomic-level simulations, we uncovered how structural heterogeneities such as interfaces, native defects, and alloying elements drive anisotropic sublimation processes. This multimodal approach elucidated the key role of defects and edge configurations in driving preferential sublimation pathways. Understanding the physics behind the formation, growth, and transformation of thermally induced defects is crucial for integrating defects as a toolkit to design tunable low-dimensional chalcogenides. The ability to engineer controlled nanopore formation opens possibilities in areas such as biosensing, gas storage/separation, and catalysis, where tunable nanoporosities and enhanced molecular binding could enable performance breakthroughs.

Please cite this article in press as: Moradifar et al., Thermally induced structural evolution and nanoscale interfacial dynamics in Bi-Sb-Te layered nanostructures, Matter (2024), https://doi.org/10.1016/j.matt.2024.08.006

crystal, extrinsic defects can be created by external stimuli, such as irradiation (electrons, ions, or laser pulses) or stress (thermal, mechanical, etc.) and further modulate the electronic, optical, and optoelectronic properties of the crystal. As an example, thermally induced polygonal defects are proposed as a tool for tuning and selective enhancement of the plasmonic response in 2D Bi_2Te_3-Sb_2Te_3 in-plane heterostructures over a broad spectral range.[8] In addition, ion irradiation-induced vacancy clusters are correlated with the formation of characteristic charged and neutral excitons in low-dimensional MoS_2 and WSe_2[9–11] as well as binding excitons and trions.[9] Similarly, extrinsic defects can modify the electronic properties, such as the band gap in transition metal dichalcogenides.[12–14]

Scanning/transmission electron microscopy (S/TEM) has enabled real-time *in situ* observation of the crystal structure, defect dynamics, and transformation pathways of various classes of materials under external stimuli in various environments with near-atomic precision. It can also be used to create or manipulate defects in real time.[15–18] There have been a few reports on exploring the phase stabilities of Ge-Sb-Te alloy[19] and sublimation of Bi_2Te_3 and Bi_2Se_3 nanocrystals under thermal stress via *in situ* TEM.[20–22] In a recent study, the impact of copper intercalation on structural transformation of Bi_2Te_3 has been investigated.[23,24] However, the role of alloying species and heterogeneities, including native point defects and presence of a heterointerface, in the sublimation pathways and structural dynamics of these layered metal chalcogenides have yet to be explored.

In this work, using *in situ* TEM with a heating stage, we assess the high-temperature structural dynamics, compositional stabilities, and real-time monitoring of thermally induced defects in hexagonal Bi_2Te_3-Sb_2Te_3 in-plane heterostructures. The results are compared with the ternary alloy counterpart of Bi_2Te_3 and Sb_2Te_3, $Sb_{2-x}Bi_xTe_3$, to further identify how the presence of a physical heterointerface and alloying elements can alter the sublimation pathways during *in situ* TEM annealing. In this study, the hexagonal platelets of Bi_2Te_3-Sb_2Te_3 in-plane heterostructures and $Sb_{2-x}Bi_xTe_3$ alloys are prepared through a two-step solvothermal method based on a Te-seeded growth (Figure S1).[6,25]

The experimental findings are further combined with density functional theory (DFT) calculations to gain atomic insight into the underlying mechanism and understand the potential thermodynamic pathways responsible for the preferential nanopore nucleation and anisotropic sublimation in Bi-Sb-Te ternary systems, including Bi_2Te_3-Sb_2Te_3 heterostructures and $Sb_{2-x}Bi_xTe_3$ alloys. Based on our *in situ* S/TEM observations and DFT calculations, we identify the most energetically favorable native defects in Bi2Te3, Sb2Te3, as well as in the SbBiTe3 alloy. Additionally, we determine the preferential edge configurations in Bi2Te3, the parent structure, that drive both polygonal nanopore formation and preferential sublimation. Understanding the physics behind the formation, growth, and transformation of thermally induced defects is of great significance to further integrate defects as a tuning toolkit for a wide range of functional properties.[13,26] Additionally, deep insight into the atomistic mechanisms governing sublimation is of great importance in guiding the field of defect-assisted optical properties and band-gap tuning and ultimately designing tunable low-dimensional chalcogenides.

RESULTS AND DISCUSSION

Bi_2Te_3 and Sb_2Te_3 both share a rhombohedral crystal structure with space group of R $\bar{3}$ m (Figure S2). Having a layered microstructure, Bi_2Te_3 and Sb_2Te_3 consist of

[1]Department of Materials Science and Engineering, Materials Research Institute, The Pennsylvania State University, University Park, PA 16802, USA

[2]Department of Materials Science and Engineering, Stanford University, Stanford, CA 94305, USA

[3]Department of Mechanical Engineering, The Pennsylvania State University, University Park, PA 16802, USA

[4]2D Crystal Consortium (2DCC), Materials Research Institute (MRI), The Pennsylvania State University, University Park, PA 16802, USA

[5]Department of Physics Engineering, Istanbul Technical University, Maslak, Istanbul, Turkey

[6]Department of Materials Science and Nano Engineering, Rice University, Houston, TX 77005, USA

[7]Department of Physics, Umeå University, 90187 Umeå, Sweden

[8]Lead contact

*Correspondence: pmoradi@stanford.edu (P.M.), nua10@psu.edu (N.A.)

https://doi.org/10.1016/j.matt.2024.08.006

Please cite this article in press as: Moradifar et al., Thermally induced structural evolution and nanoscale interfacial dynamics in Bi-Sb-Te layered nanostructures, Matter (2024), https://doi.org/10.1016/j.matt.2024.08.006

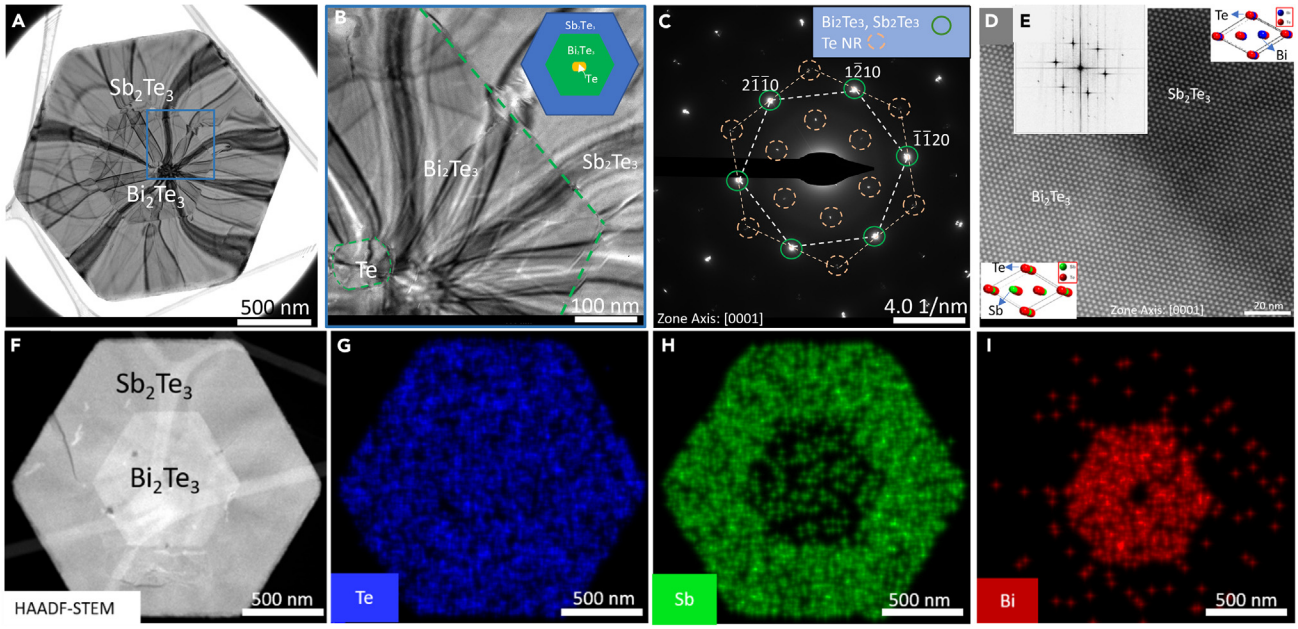

Figure 1. Structural characterization of the Bi_2Te_3/Sb_2Te_3 heterostructure

(A) TEM image of Bi_2Te_3/Sb_2Te_3 in-plane heterostructures displaying bending contours.

(B) Magnified TEM image of the heterointerface area marked in (A), displaying the bend contour formation, originating from the central Te nanorod region.

(C) EDP of the heterostructure (A) along the [0001] direction, exhibiting diffraction from the Sb_2Te_3 and Bi_2Te_3 regions and Te nanorod.

(D and E) HRSTEM and FFT of a heterointerface region (Bi_2Te_3/Sb_2Te_3) along the [0001] direction.

(F) HAADF-STEM image of where chemical composition maps are acquired from.

(G) Te XEDS chemical composition map confirming a uniform distribution of Te atoms in the Sb_2Te_3 and Bi_2Te_3 regions.

(H) Sb XEDS chemical composition map confirming the composition of the Sb_2Te_3 region.

(I) Bi XEDS chemical composition map confirming the composition of the Bi_2Te_3 region (the central Bi-deficient region is due to the Te seeded growth process). See also Figures S1–S4 and Table S1.

alternative hexagonal monoatomic crystal planes of Bi and Te atoms that are arranged with ABC ordering along the c axis. Five monoatomic layers with the quint substructure of Te_1-Bi-Te_2-Bi-Te_1 form a tightly bound quintuple (QL) sheets that is charge neutral with a thickness of 1 nm. The layered structure of Bi_2Te_3 features strong intralayer covalent bonds between Bi and Te while experiencing weak interlayer van der Waals forces.[3,25,27,28]

Figure 1 shows TEM structural analysis of 2D Bi_2Te_3-Sb_2Te_3 in-plane heterostructures, confirming the single crystallinity of the hexagonal nanocrystals. Bright-field TEM of a 2D Bi_2Te_3-Sb_2Te_3 in-plane heterostructure on a lacey carbon grid (Figure 1A) reveals a ripple-like pattern indicating the existence of bent contours in this structure. The bent contours potentially originate from the local and inhomogeneous distribution of elastic strain, as observed previously in solvothermally processed Bi_2Te_3 nanoplates.[28,29] Here, the presence of the heterointerfaces is also expected to further contribute to the formation of bent contours in the nanoplatess. According to Figures 1A and 1B, bent contours initiate from the proximity of a Te nanorod at the center of the nanoplate. The electron diffraction pattern (EDP) of the entire nanoplate along the [0001] direction shows that the 2D in-plane heterostructure is single crystalline (Figure 1C) with Bi_2Te_3 and Sb_2Te_3 diffraction spots overlapped. The extra spots marked with orange circles are associated with the Te nanorod from the same zone axis at the center of the nanoplate. This observation is consistent with the simulated EDPs for the Te nanorod, Bi_2Te_3, and Sb_2Te_3

Please cite this article in press as: Moradifar et al., Thermally induced structural evolution and nanoscale interfacial dynamics in Bi-Sb-Te layered nanostructures, Matter (2024), https://doi.org/10.1016/j.matt.2024.08.006

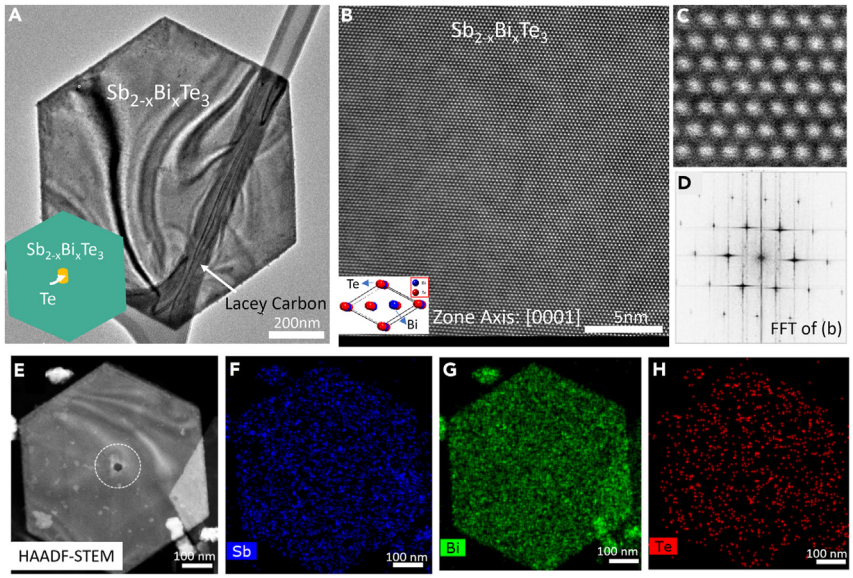

Figure 2. Structural characterization of the Bi-Sb-Te ternary alloy

(A) TEM image of a 2D $Sb_{2-x}Bi_xTe_3$ alloy displaying bent contours originating from a lacey carbon/nanoplate interface.

(B and C) HRSTEM of a 2D $Sb_{2-x}Bi_xTe_3$ alloy at two different magnifications along the [0001] zone axis.

(D) FFT of the HRSTEM image in (B).

(E) HAADF-STEM image of where the chemical composition maps are acquired from.

(F) Sb XEDS chemical composition map with a uniform distribution over the nanoplate.

(G) Bi XEDS chemical composition with a uniform distribution over the nanoplate.

(H) Te XEDS chemical composition with a uniform distribution over the nanoplate. See also Figures S5 and S6.

structures (Figures S3 and S4). However, due to the small lattice mismatch between Bi_2Te_3 and Sb_2Te_3, the spots overlap slightly and is elongated in both the simulations and the experimental observations shown in Figure 1C. The lattice parameters for Bi_2Te_3 and Sb_2Te_3 are $a_{Bi2Te3} = b_{Bi2Te3} = 4.384$ Å, $c_{Bi2Te3} = 30.487$ Å, $a_{Sb2Te3} = b_{Sb2Te3} = 4.264$ Å, and $c_{Sb2Te3} = 30.458$ Å[30] and are listed in Table S1. The lattice mismatch between Bi_2Te_3 and Sb_2Te_3 is about 2.5%. The lattice mismatch between Bi_2Te_3 and Sb_2Te_3 (in the x-y lattice plane) is expected to minimize the strain energy through the presence of compressive or tensile elastic in-plane strain.[30,31]

The presence of a near-atomically sharp heterointerface between Bi_2Te_3 and Sb_2Te_3 is confirmed using high-angle annular dark field (HAADF)-STEM imaging of the heterointerface region and the corresponding fast Fourier transform (FFT), as shown in Figures 1D and 1E. The chemical composition of the Bi_2Te_3-Sb_2Te_3 in-plane heterostructure shows the distribution of Te over the entire sample region, while Bi and Sb are in the inner and outer regions of the heterostructure, respectively (Figure 1F–1I). The Bi deficiency in the central region of the nanoplate (Figure 1I) is due to the growth process of the heterostructure, starting from Te nanorods. All images presented in Figure 1 were acquired under static condition at room temperature (RT) and accelerating voltage of 80 kV. Figure 2 shows 2D $Sb_{2-x}Bi_xTe_3$ alloy heterostructures with no interface (see Figure S5 for the EDP acquired from the nanoplate in Figure 2A). Bent contours are observed on multiple regions of the sample but do not originate from the central part of the sample, contrary to the Bi_2Te_3-Sb_2Te_3 in-plane heterostructures (Figure 1A and 1B), in which the bend contours initiate from the central area inside Bi_2Te_3 and continue toward the outer edge of the nanoplate. Figure 2B and 2C show

Please cite this article in press as: Moradifar et al., Thermally induced structural evolution and nanoscale interfacial dynamics in Bi-Sb-Te layered nanostructures, Matter (2024), https://doi.org/10.1016/j.matt.2024.08.006

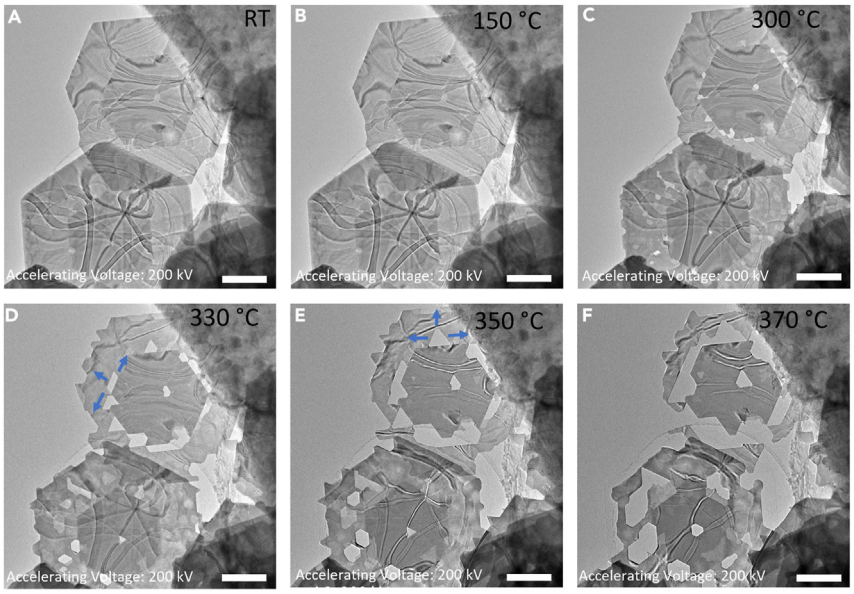

Figure 3. Temperature-dependent structural dynamics and sublimation pathways in the Bi_2Te_3/Sb_2Te_3 heterostructure

(A–F) TEM images of low-dimensional Bi_2Te_3/Sb_2Te_3 heterostructure nanoplates at RT, 150°C, 300°C, 330°C, 350°C, and 370°C, respectively, indicating the strain relaxation and preferential nanopore defect formation in the center, at the heterointerface, and at the outer edges of the structure. Blue arrows indicate the growth direction of the polygonal nanopores including both triangular and quasi-hexagonal nanopores. The scale bars are 500 nm. Images were taken using an accelerating voltage of 200 kV. See also Figures S7 and S8.

high-resolution STEM (HRSTEM) images taken at two different magnifications of the 2D $Sb_{2-x}Bi_xTe_3$ alloy along the [0001] zone axis with no evident trace of defects or phase segregation. The FFT pattern of the 2D $Sb_{2-x}Bi_xTe_3$ alloy from this region also shows a clear pattern of a single-crystal alloy (Figure 2D). The XEDS (energy-dispersive X-ray spectroscopy) chemical analysis of this nanoplate shows a uniform distribution of Sb, Bi, and Te at RT across the nanoplate (Figures 2E–2H). The marked region in Figure 2E should contain Te nanorods with no Bi and Sb content. To observe this compositional variation, a longer acquisition time for the XEDS map is required to see whether this area indeed has higher Te content than its surroundings. Figure S6 displays the two FFTs from Figures 1E and 2D superimposed in different colors. As seen from the FFTs (Figure S6), these two structures (alloy vs. heterostructure) have similar crystal structures and *d* spacings.

To understand the structural dynamics, *in situ* TEM observations are conducted at elevated temperatures (Figure S7 for a TEM image of the sample on an *in situ* TEM heating device). The thermally driven structural dynamics can be seen in Video S1, which plays the sequential frames of the Bi_2Te_3-Sb_2Te_3 heterostructure acquired between 300°C and 390°C at 200 kV. In addition, selected frames of the video are shown in Figures 3A–3F, showing the sublimation process in the Bi_2Te_3-Sb_2Te_3 in-plane heterostructure with a heating rate of 5°C/min. The details of the experimental parameters and imaging conditions are included in the experimental procedures. The formation of polygonal defects (nanopores) is initiated at the outer edges, Bi_2Te_3/Sb_2Te_3 heterointerface, and the center of the Bi_2Te_3 with the rich Te core. Edges are some of the energetically favorable sites for sublimation due to the presence of the reactive dangling bonds and variations in bonding configurations.[20] In

Please cite this article in press as: Moradifar et al., Thermally induced structural evolution and nanoscale interfacial dynamics in Bi-Sb-Te layered nanostructures, Matter (2024), https://doi.org/10.1016/j.matt.2024.08.006

addition, interfacial mismatch strain can induce localized structural instabilities, thus making heterointerfaces, such as the Bi_2Te_3/Sb_2Te_3, Bi_2Te_3/Te heterointerface, energetically favorable for the initiation of sublimation. In general, strained regions (elastic or plastic strain) can act as highly reactive areas with high thermal stress that can lead to the formation and growth of polygonal nanopores at elevated temperatures.[14,32] Overall, we speculate that, under thermal stress, the high density of point defects at the Te core, interfacial mismatch strain, and chemical bonding inhomogeneities at the interfaces act as localized and reactive nanoregions that can initiate the sublimation process.

In the following sections, we further link the observations on the anisotropic sublimation to the role of pre-existing point defects, various edge configurations, and edge formation energies. Triangular and quasi-hexagonal nanopores are the dominant polygonal configurations observed through sublimation. However, transformation of nanopores can also take place, as shown in Figure 3. A transformation from a triangular configuration to a quasi-hexagonal configuration is realized for the nanopores in the Te-rich core, while a reverse transformation from a quasi-hexagonal configuration to a triangular configuration occurs for the nanopores at the heterointerface. Additionally, with a further increase in temperature, these nanopore defects coalesce with the adjacent polygonal nanopores and form larger nanopores.

It is worth noting that electron beam irradiation can act as an external stimulus to trigger defect formation and growth. Therefore, to eliminate the beam effect on the formation of defects during the sublimation process, the electron beam is blanked during the *in situ* annealing process, and the specimen is only illuminated when capturing an image. To confirm that thermal annealing is the dominant external stimulus behind sublimation, a comparative *in situ* annealing experiment is performed at a lower accelerating voltage of 80 kV. Thermally driven *in situ* structural dynamics in the Bi_2Te_3-Sb_2Te_3 in-plane heterostructure at 80 kV between 300°C and 390°C at 80 kV are shown in Video S2, with selected frames of the dynamics shown in Figure 4. The Bi_2Te_3-Sb_2Te_3 in-plane heterostructure at 80 kV remains stable up to 300°C before the polygonal defects start forming. With further temperature increase, the preferential sublimation of prismatic {01 $\bar{1}$ 0} planes, such as (1$\bar{1}$ 00), (10$\bar{1}$ 0), and ($\bar{1}$ 010), starts to occur. We observe the preferential sublimation of the edge planes of the nanoplate to be mainly responsible for the formation of polygonal defects. With similar observations at 80 kV and 300 kV, these experiments rule out the effect of beam energy on the microstructure evolution of the nanoplate, thus indicating the defects to be thermally driven and through the sublimation process. Figure S7C shows a 3D schematic of the hexagonal Bi_2Te_3-Sb_2Te_3 in-plane heterostructures and $Sb_{2-x}Bi_xTe_3$ alloy, displaying the crystallographic orientation of planes (zone axis: [0001]). This figure serves as a reference to identify the preferential sublimation planes during *in situ* TEM heating. The details on the imaging condition are included in the experimental procedures.

To understand how the presence of the heterointerface can alter the sublimation pathways and the sublimation starting temperature, a comparative study is performed on the $Sb_{2-x}Bi_xTe_3$ ternary alloy with no heterointerface present. Thermally driven *in situ* structural dynamics in $Sb_{2-x}Bi_xTe_3$ between 300°C and 400°C are shown in Video S3, with selected frames of these dynamics shown here. Figure 5 presents the structural evolution upon *in situ* annealing of the $Sb_{2-x}Bi_xTe_3$ alloy between 310°C and 380°C. Selective frames of the sequential sublimation process are shown in Figures 5A–5H. Similar to the heterostructure, anisotropic and preferential

Please cite this article in press as: Moradifar et al., Thermally induced structural evolution and nanoscale interfacial dynamics in Bi-Sb-Te layered nanostructures, Matter (2024), https://doi.org/10.1016/j.matt.2024.08.006

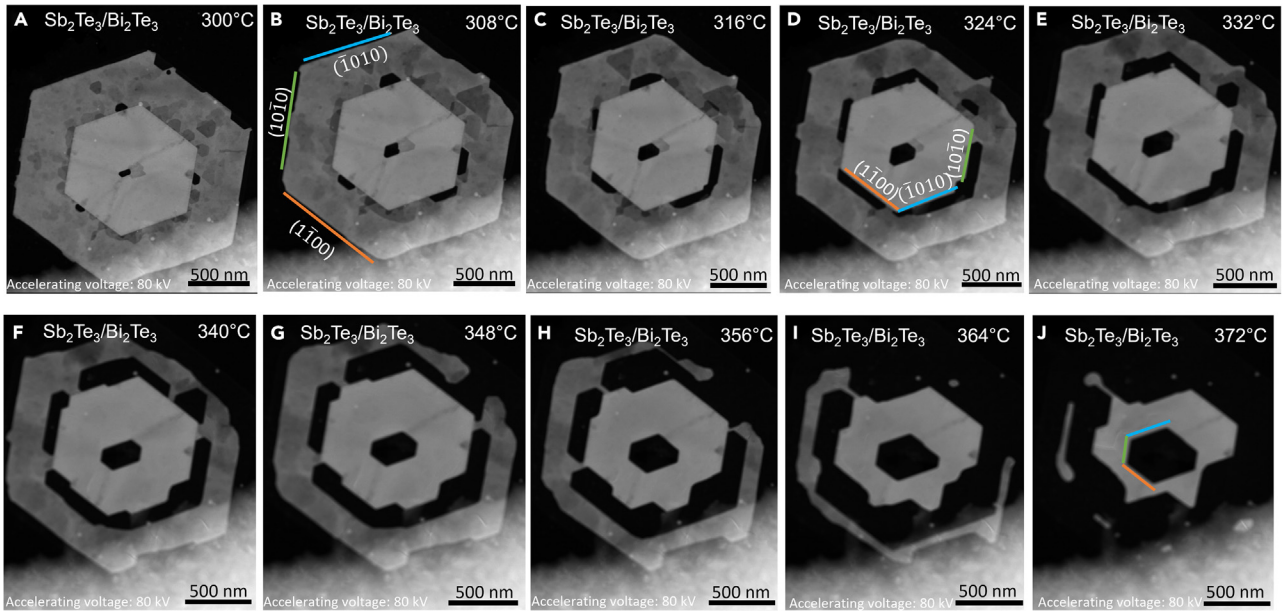

Figure 4. Sublimation pathways, including polygonal defect formation, growth, and coalescence, in the Bi_2Te_3/Sb_2Te_3 heterostructure

(A–J) HAADF-STEM images of low-dimensional Bi_2Te_3/Sb_2Te_3 heterostructure nanoplates at 300°C, 308°C, 316°C, 324°C, 332°C, 340°C, 348°C, 356°C, 364°C, and 372°C, illustrating the sublimation of the heterostructure through formation of preferential triangular and hexagonal nanopores in the center, at the heterointerface, and at the outer edges of the structure. Image acquisition was done with an 8°C interval and 2 seconds exposure time/frame. Images were taken using an accelerating voltage of 80 kV.

sublimation of prismatic {01 $\bar{1}$ 0} planes are observed, as shown in Figures 5A, 5B, 5E, and 5H. Major differences are observed during sublimation of the $Sb_{2-x}Bi_xTe_3$ alloy in comparison with the Bi_2Te_3-Sb_2Te_3 in-plane heterostructure. First, the sublimation starts at a higher temperature of around 320°C as opposed to 300°C for Bi_2Te_3-Sb_2Te_3 in-plane heterostructures, which can be attributed to the interfacial mismatch strain between Bi_2Te_3 and Sb_2Te_3 that can significantly impact the sublimation pathway. In contrast, in the $Sb_{2-x}Bi_xTe_3$ (nominal x = 1) alloy, there is no heterointerface and, therefore, no interfacial strain. We observe no polygonal defects to form inside the $Sb_{2-x}Bi_xTe_3$ alloy nanoplate, and the sublimation only takes place along the outer edges. Further in the sublimation process, a transformation from a hexagonal nanoplate (Figure 5A) to a triangular nanoplate (Figure 5H) is observed. The hexagonal $Sb_{2-x}Bi_xTe_3$ alloy nanoplates evolve to triangular nanoplates, retaining the low-energy facets, with 60° rotation with respect to their pristine form. The lack of internal sublimation of the alloy sample can be explained by the uniformity of the sample and reduced amount of internal local strain. Although sublimation is driven by chalcogenide depletion, this nanoscale study shows that (1) lattice mismatch, (2) strain at heterointerfaces, and (3) local structural inhomogeneities can accelerate the sublimation process and determine preferential sites for anisotropic sublimation.

The *in situ* TEM observations in Figures 4 and 5 indicate that preferential sublimation is initiated at the edges. Additionally, we can observe layer-by-layer sublimation that is identified by contrast variations on the nanoplates during sublimation, which can be seen in Videos S1, and S2, and Figure 5. By increasing the temperature, the surface energy increases further because of an increase in the number of uncoordinated sites as well as surface roughening, which will accelerate the sublimation rate.[33,34] By increasing the temperature, the atoms can also escape through the surface,

Please cite this article in press as: Moradifar et al., Thermally induced structural evolution and nanoscale interfacial dynamics in Bi-Sb-Te layered nanostructures, Matter (2024), https://doi.org/10.1016/j.matt.2024.08.006

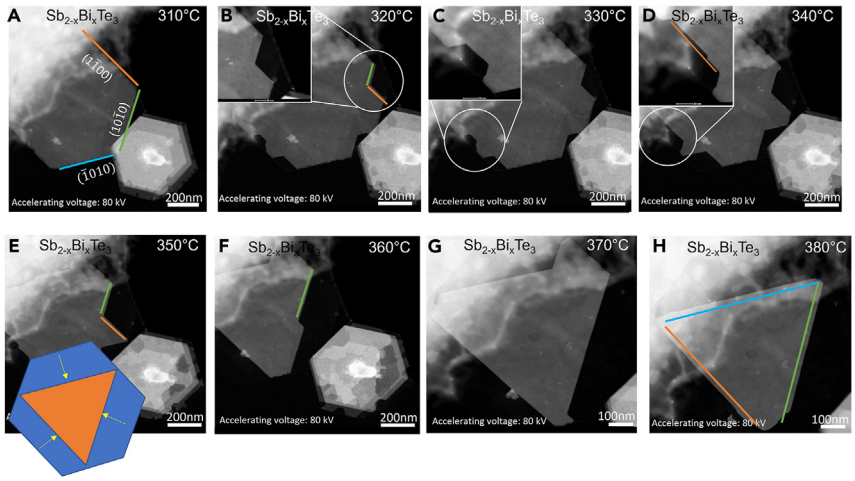

Figure 5. Sublimation pathways, including edge evolution and hexagon-triangle transformation, in the Bi-Sb-Te ternary alloy

(A–K) HAADF-STEM images of low-dimensional $Sb_{2-x}Bi_xTe_3$ alloy nanoplates at 310°C, 320°C, 330°C, 340°C, 350°C, 360°C, 370°C, 380°C, and 390°C, respectively. Hexagonal nanoplates evolve to triangular nanoplates with 60° rotation with respect to their pristine form through preferential sublimation of prismatic {01 $\bar{1}$ 0}. Image acquisition was done with a 10°C interval and 2 seconds exposure time/frame. Images were taken using an accelerating voltage of 80 kV See also Figure S9.

promoting a layer-by-layer sublimation, which is observed simultaneously with the edge sublimation at higher temperatures.

Among different atomic species, the sublimation is, however, governed by Te atoms. Sublimation of Te and depletion of chalcogenide species at higher temperatures in Bi-Sb-Te layered nanostructures is due to the combined effect of weak interaction forces between the Te_1-Te_1 layer in the Bi_2Te_3 and Sb_2Te_3 nanostructures as well as high vapor pressure of Te (179°C at 10^{-7} mbar vapor pressure) in comparison with other elemental species in the structure (Bi and Sb). Our *in situ* TEM observation leads us to the phenomenological explanation that, in Bi-Te-Sb heterostructures, the sublimation starts with Te dissociation from uncoordinated or low-coordinated sites, move to the surface, and ultimately volatilize from the surface. The sublimation of Te from the structure leaves Te dangling bonds to further facilitate the dissociation of Te from the structure, resulting in preferential growth of polygonal defects in the center, at the outer edges, and in the heterointerface region. Ultimately, the continuous Te loss from the structure leaves excess Bi behind forming a Bi bulb, as shown in XEDS chemical composition maps acquired at ~360°C and ~370°C (Figures S8 and S9). This observation validates the prior hypothesis that Te dissociation is the root cause for structural failure after plastic deformation and post annealing in ternary TE bulk systems of $Bi_{0.4}Sb_{1.6}Te_3$[35,36] and $Pb_{(1-x)}Sn_xTe$.[21]

High surface energy density in nanoplates, originating from large surface-to-volume ratio, as well as large numbers of uncoordinated and/or low-coordinated sites lowers the thermal activation barrier for sublimation thus lower the sublimation temperature in nanoplates compared to their bulk counterparts.[37] *In situ* TEM is a powerful tool for enabling direct observation and identifying the sublimation mechanisms in these structures. While not the focus of this paper, it is worth mentioning that mass spectrometry (MS) is a promising complementary technique for understanding the sublimation kinetic pathways. MS enables quantitative measurement of the temperature-dependent weight loss and identification of the temperature-dependent

Please cite this article in press as: Moradifar et al., Thermally induced structural evolution and nanoscale interfacial dynamics in Bi-Sb-Te layered nanostructures, Matter (2024), https://doi.org/10.1016/j.matt.2024.08.006

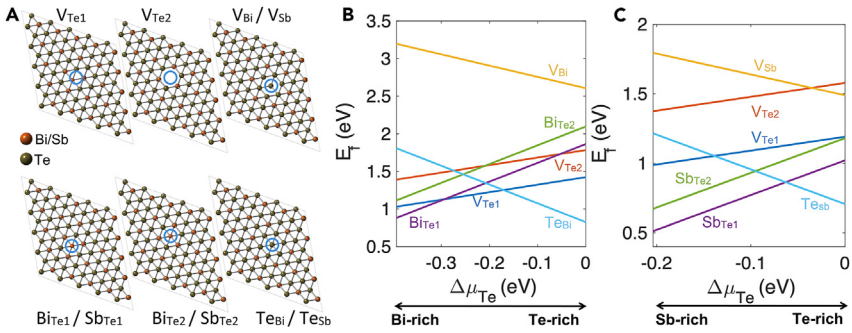

Figure 6. Native point defect configurations and formation energies in Bi_2Te_3 and Sb_2Te_3

(A) Native point defect configurations, including atomic vacancies and antisite defects.

(B) Defect formation energies of vacancy and antisites defects in Bi_2Te_3 (1 QL layer) as a function of chemical potential of Te. Te_{Bi} antisites are dominant defects under Te-rich/Bi-poor conditions. See also Figures S11 and S12.

sublimation rate. Such measurement is important for establishing a quantitative comparison among low-dimensional materials and their bulk counterparts. Finally, it is worth noting the thickness of nanoplates, surface atomic rearrangement during sublimation, initial particle size, morphology, and additional surface asperities (i.e., strain, contamination, or presence of ligand and surfactants), and the distribution of uncoordinated sites can further impact the sublimation temperature.[33,37]

In our experiments, we are looking at a stack of QLs that are bonded by a weak van der Waals interaction between the Te_1 atomic layers. QLs are building blocks of Bi_2Te_3 and Sb_2Te_3 structures. Each QL is approximately 1 nm thick and consists of 5 atomic layers, (Te_1-Bi-Te_2-Bi-Te_1). To further identify the thickness of the nanoplates, electron energy loss spectroscopy (EELS) datasets of pristine nanoplates at RT are used. We used STEM-EELS in a dual-EELS configuration. Using the log-ratio approach, the ratio between thickness (t) to inelastic mean free path of electrons (λ) transmitting through the sample, t/λ, is an indicator of the average number of scattering events per incident electron and is correlated with the ratio of the total intensity of the EELS spectrum to the total intensity of the zero-loss spectrum ($t/\lambda = -\ln(I_0/I_t)$). The t/λ is measured between 0.16 and 0.19 (Figure S10), in which I_0 is the intensity of elastically or quasi-elastically scattered electrons, and I_t is the total transmitted intensity of electrons through combined elastically and inelastically scattered events.

Furthermore, intrinsic defects, native defects, play a vital role in mechanisms and pathways governing sublimation as a first-order phase transition. DFT calculations are conducted to provide atomic-level insight into the structural dynamics and edge evolution during the defect-aided sublimation. Possible native point defects (vacancies and antisites) as well as various point defect configurations in 2D Bi_2Te_3, Sb_2Te_3, and $BiSbTe_3$ structures are shown in Figures 6 and 7, respectively. The associated defect formation energies in Bi_2Te_3 and Sb_2Te_3 as a function of Te chemical potential are plotted in Figures 6B and 6C. Similarly, the defect formation energies in the Bi-Sb-Te alloy structure ($BiSbTe_3$) are calculated, as shown in Figure 7B.

The calculations reveal that, under both Bi(Sb)-rich and Te-rich condition in $Bi(Sb)_2Te_3$, and under both Sb-rich and Bi-rich condition in $BiSbTe_3$ alloyed structure, antisite defects are the dominant native defects. It is worth noting that Bi-rich refers to the chemical potential of Bi [μ_{Bi}] in a bulk α-Bi [μ_{Bi}^0] [i.e., $\Delta\mu_{Bi} = \mu_{Bi} - \mu_{Bi}^0 = 0$];

Please cite this article in press as: Moradifar et al., Thermally induced structural evolution and nanoscale interfacial dynamics in Bi-Sb-Te layered nanostructures, Matter (2024), https://doi.org/10.1016/j.matt.2024.08.006

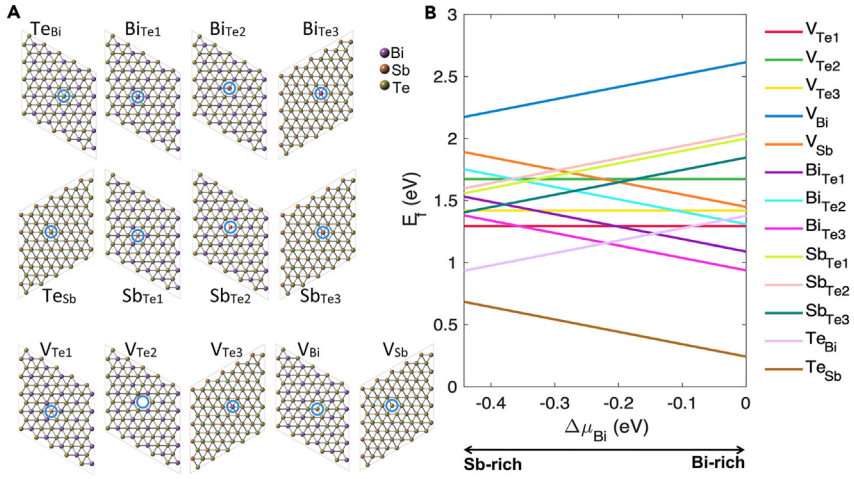

Figure 7. Native point defect configurations and formation energies in the Bi-Sb-Te ternary alloy

(A) Native point defect configurations, including Bi, Sb, and Te atomic vacancies and various antisite defects (e.g.,Te_{Bi} and Te_{sb}).

(B) Defect formation energies in $BiSbTe_3$ as a function of chemical potential of Bi under the Te-rich condition. Te_{sb} antisites are dominant defects under the Te-rich and Bi-rich/Sb-poor growth condition.

Sb-rich refers to the chemical potential of Sb [μ_{Sb}] in a bulk α-Sb [μ_{Sb}^0] [i.e., $\Delta\mu_{Sb} = \mu_{Sb} - \mu_{Sb}^0 = 0$]; Te-rich means the chemical potential of Te [μ_{Te}] in a bulk α-Te [μ_{Te}^0] [i.e., $\Delta\mu_{Te} = \mu_{Te} - \mu_{Te}^0 = 0$]). This is consistent with the previous findings by Scanlon et al.,[38] who showed that the antisite defects play a key role in controlling the bulk conductivity of topological insulators.[38] Our DFT calculations further reveal, in Bi_2Te_3 nanoplates under the Te-poor condition, that the Bi_{Te1} antisite defect where Te is replaced by Bi possesses the lowest formation energy among all native defects, while under the Te-rich condition, the Te_{Bi} antisite defect in which an excess Te occupies the Bi site is the most energetically favorable point defect. In the Sb_2Te_3 structure, an analogous phenomenon is observed. Under the Te-rich condition, Te_{Sb} antisite defects in which Te occupies the Sb sites require the lowest defect formation energy.

The major difference that is observed in Bi_2Te_3 compared to bulk Bi_2Te_3 is that, in a Bi_2Te_3 QL, for $\Delta\mu_{Te}$ in the range of −0.28 to −0.16 eV, the vacancy defect V_{Te1} is the most energetically favorable. This is different from that for bulk Bi_2Te_3, where the formation energies for all three types of vacancies (V_{Bi}, V_{Te1}, and V_{Te2}) are found to be much higher than that for antisites in both Te-rich and Bi-rich conditions.[39] However, in Sb_2Te_3 and $BiSbTe_3$ structures, antisites consistently emerge as the most energetically favorable defects across the entire range of $\Delta\mu_{Te}$ or $\Delta\mu_{Bi}$ for Sb_2Te_3 and $BiSbTe_3$ respectively. Because of the abundance of Te through the synthesis procedure, due to the epitaxial nucleation and growth of Bi_2Te_3/Sb_2Te_3 on the surface of Te nanorods, we speculate that the presented in-plane Bi_2Te_3-Sb_2Te_3 heterostructure and $Sb_{2-x}Bi_xTe_3$ alloy in our study are representing a Te-rich scenario; therefore, Te_{Bi} and Te_{Sb} antisites defects are the most dominant native defects present in these structures at room temperature. Since an excess Te atom weakly interacts with the two adjacent Te host atoms in the lattice, as compared to the Bi-Te or Sb-Te covalent bond, we expect that the presence of Te_{Bi} and Te_{Sb} antisites further promotes Te sublimation.

Finally, various atom detachment pathways can result in formation of different types of edge structures during sublimation. The edge configurations are mediated by the

Please cite this article in press as: Moradifar et al., Thermally induced structural evolution and nanoscale interfacial dynamics in Bi-Sb-Te layered nanostructures, Matter (2024), https://doi.org/10.1016/j.matt.2024.08.006

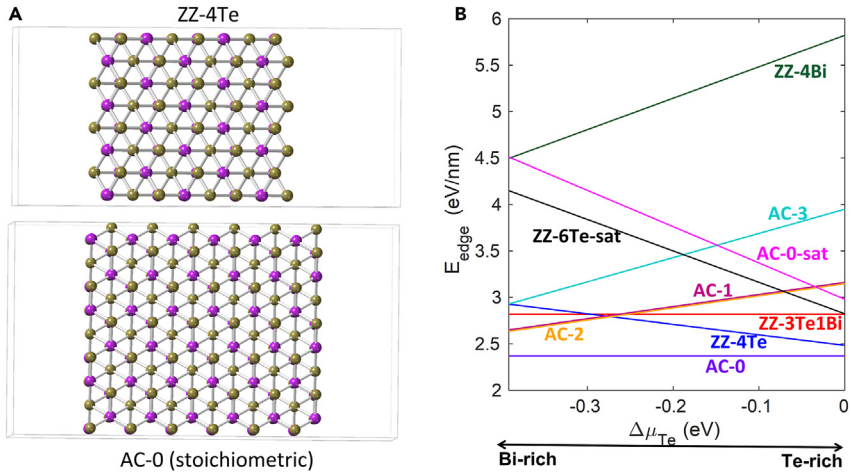

Figure 8. Edge configurations and edge formation energies in one Bi_2Te_3 QL layer

(A) Examples of stable ZZ (ZZ-4Te) and armchair (AC-0) edge configurations in one Bi_2Te_3 QL layer.

(B) Formation energies for different types of ZZ and armchair edge configurations. See also Figure S13.

chemical potential difference between Bi and Te in Bi_2Te_3 QL. Eight edge models are generated and selectively presented in Figures S11–S13: zigzag (ZZ) edges with Te and/or Bi terminations (ZZ-4Te, ZZ-3Te1Bi, ZZ-4Bi, and ZZ-6Te-sat [fully saturated]) and armchair edges (AC-0 [stoichiometric], AC-0-sat [fully saturated], AC-1, AC-2, and AC-3). Each model is allowed to relax to its ground state. The two most energetically favorable edge configurations, ZZ-4Te and AC-0, are shown in Figure 8A.

Figure 8B presents the edge formation energies as a function of the excess of chemical potential of Te ($\Delta\mu_{Te}$). The formation energy for the stoichiometric armchair edge (AC-0) is a constant number with respect to the Δu_{Te}, and it is also thermodynamically most stable in allowed Te chemical potential, indicating that the morphology of Bi_2Te_3 should be dominated by the AC-0 edge during the growth. The next energetically favorable edge is the ZZ-4Te in the Te-rich condition and armchair edge AC-2 in the Bi-rich condition. The formation energy for the ZZ-4Bi edge is always the highest across the entire range of $\Delta\mu_{Te}$, indicating that ZZ-4Bi is less likely to be formed during growth, while the formation of other edges, like AC-3, AC-0-sat, ZZ-6Te-sat, AC-1, and AC-2 is highly correlated to $\Delta\mu_{Te}$ (Te-rich or Bi-rich condition).

Thermodynamically, slow-growing edges are the most stable ones and therefore the most energetically favorable during growth and dominate the growth morphology. However, during sublimation and etching, it is expected that the fast-growing edges with higher formation energies govern both the sublimation process and the nanopore morphology. The hexagonal morphology of the nanoplate as the equilibrium shape at RT for both the alloy and heterostructure can further confirm that the armchair edges (AC-0) are the most stable edges at RT. It is expected that, at higher temperatures, both the ZZ edges (ZZ-4Bi and ZZ-6Te-sat) and armchair edges (AC-3 and AC-0-sat) could be the more stable edges. This is consistent with the sublimation observations that are shown in Figure 5, displaying a hexagonal-to-triangular transformation for the alloy structure at higher temperatures.

In this work, we focused on Bi-Sb-Te system as a topological insulator parent system. To our knowledge, this is the first time that we can directly observe the sublimation pathways and link the nanoscale structural dynamics to a series of heterogeneities, including

Please cite this article in press as: Moradifar et al., Thermally induced structural evolution and nanoscale interfacial dynamics in Bi-Sb-Te layered nanostructures, Matter (2024), https://doi.org/10.1016/j.matt.2024.08.006

the heterointerface, and native point defects in ternary metal chalcogenide systems. This work provides an in-depth understanding and establishes a combined experiment-theory framework based on *in situ* TEM and DFT that can be extended to understand a wide range of van der Waals (vdW) ternary chalcogenide systems. As derivatives of the Bi_2Te_3 structure, in Mn-Bi-Te systems, Mn can form a sublattice resulting in a septuple-layer building block. In Mn-Bi-Te systems, atomic layers are stacked in the Te-Bi-Te-Mn-Te-Bi-Te sequence, while in Cr-Ge-Te systems, Cr atoms are sandwiched between Te atoms, forming building blocks of Te-Ge-Cr-Ge-Te.[40,41] Emerging 2D vdW magnets based on the Mn-Bi-Te system and phase-change materials based on Cr-Ge-Te and Ge-Sb-Te systems are of particular interest, in which structural heterogeneities and thermal conductivity are key features for optimizing the performance metrics.[42,43] Finally, our work provides a proposed pathway for nanopore engineering using thermally induced polygonal defects in vdW-layered metal chalcogenide systems, which is of particular interest in biosensing to improve selectivity or enhance biomolecule binding as well as in the gas storage (e.g., hydrogen storage, carbon capture, or gas separation) research domains.

Conclusion

We have reported the direct observation of sublimation dynamics pathways in a Bi_2Te_3-Sb_2Te_3 in-plane heterostructure and its ternary alloy counterpart via *in situ* TEM at elevated temperatures. Microstructural evolution consisted of formation, growth, and coalescence of thermally induced nanopores and, ultimately, preferential sublimation initiating at reactive regions with structural heterogeneities. The preferential sublimation sites are the center, heterointerface, and outer edges for the heterostructure and only outer edges for the alloy counterpart. Excessive Te in the center of the structure and a high density of defects on the heterointerface are anticipated to be the main driving force for preferential depletion of chalcogenide (Te) from these reactive sites. Triangular and quasi-hexagonal configurations are observed to be the dominant nanopore configurations, but transformation between different configurations and layer-by-layer sublimation are also reported. Furthermore, DFT calculations show that antisite defects (Te_{Sb} and Te_{Bi}), in which excess Te occupies the Sb lattice sites (in $SbTe_3$ and $BiSbTe_3$) and Bi lattice sites (in Bi_2Te_3), possess the lowest formation energy and, therefore, are the most energetically favorable and are expected to be the dominant native defects playing a key role on the sublimation process. In addition, based on the calculated edge formation energies for Bi_2Te_3 as the parent structure, it is expected that, at higher temperatures, both the ZZ edges (ZZ-4Bi and ZZ-6Te-sat) and armchair edges (AC-3 and AC-0-sat) are the more stable edges of choice. An in-depth understanding of the nanoscale dynamics is the key for making tunable layered metal chalcogenides with extended functionalities from optoelectronic devices to efficient catalysis and energy conversion. Furthermore, thermally induced defects as physical inclusions can provide pathways offering further tunability in these systems.

EXPERIMENTAL PROCEDURES

Materials

Preparation of the Bi_2Te_3-Sb_2Te_3 in-plane heterostructure and $Sb_{2-x}Bi_xTe_3$ alloy

Hexagonal 2D Bi_2Te_3 nanoplates are synthesized using a solution-phase solvothermal process and based on Te-seeded growth. Tellurium oxide (TeO_2) and bismuth oxide (Bi_2O_3) were used as the major precursors for this synthesis, matching the stoichiometry ratio at 180°C. A dispersed solution is acquired by mixing and stirring the following components, based on the reported ratio and concentration at 100°C: 0.48 g of polyvinylpyrrolidone, 30 mL ethylene glycol, 15 mM sodium hydroxide,

1.7 mM TeO_2, and 0.6 mM Bi_2O_3. The solution is further annealed at 180°C for 15 h. A schematic of Bi_2Te_3 nanosheet nucleation and growth from the surface of Te nanorods is included in Figure S2. The material is then washed thoroughly via deionized (DI) water following an immediate freeze-drying procedure to prevent oxidation. The Bi_2Te_3 nanosheets are kept under an inert atmosphere of argon inside the glovebox. For $Sb_{2-x}Bi_xTe_3$ alloy synthesis, the antimony oxide (Sb_2O_3) precursor is mixed simultaneously with the Bi_2O_3 precursor at a 1:1 ratio. However, for Bi_2Te_3-Sb_2Te_3 heterostructure synthesis, Bi_2Te_3 nanosheets are used as seeds to grow Sb_2Te_3 on the outer edges of Bi_2Te_3, during which Sb_2O_3 and TeO_2 as precursors are used for the growth of Sb_2Te_3 (6).[25]

Characterization (instrumentation and data acquisition)

TEM samples are prepared using solvent-assisted exfoliation (a 1:1 mixture of isopropyl alcohol and DI water) followed by 30–45 min of sonication to acquire a clear solution. A drop of the clear solution is dropped over a fusion *in situ* TEM heating device and dried at RT. A Talos F200X STEM equipped with a heating stage and a super XEDS detector at an accelerating voltage of 80 kV are used to acquire cross-sectional STEM images and XEDS maps. Microstructural evolution of the in-plane Bi_2Te_3-Sb_2Te_3 heterostructure and $Sb_{2-x}Bi_xTe_3$ alloy is studied using HAADF-STEM and TEM imaging techniques combined with the EDP. Chemical compositions of the nanoplates are further evaluated using XEDS. To minimize the electron beam irradiation and prevent beam-induced defects, mainly knock-on damage in this case, *in situ* experiments are mainly carried out at 80 kV. However, a comparative *in situ* TEM study is carried out at 200 kV for the Bi_2Te_3-Sb_2Te_3 heterostructure. During annealing, the electron beam is blanked to ensure that structural dynamics are dominantly a function of thermal annealing and to minimize the electron beam irradiation effect. The *in situ* annealing experiments are performed under a vacuum with no chemical agent. Experimental parameters, such as heating rate (5°C/min) and exposure time (2 s) per frame, were kept consistent with the *in situ* annealing experiments at 200 kV.

DFT simulation

All calculations for the energies of native defects and edges for 2D Bi_2Te_3 QL are carried out in the framework of DFT[44] implemented in the Vienna Ab initio Simulation Package[45,46] using the projector augmented wave[47] method and the Perdew-Burke-Ernzerhof[49] generalized gradient approximation[48] exchange-correlation energy functional. A 5 × 5×1 supercell of the 2D Bi_2Te_3 QL structure is generated and then used to create single defects, including vacancies and antisites. All structures are fully relaxed with a force criterion of 0.01 eV/Å/atom. The energy cutoff for the plane-wave basis is set to be 450 eV, and the Monkhorst-Pack k-point is 4 × 4×1 for calculating free energies of the pristine and defect structures. The formation energy for the defect structure is obtained using Equation 1, where E_{defect} and $E_{pristine}$ are the energy of one supercell (1 QL) with and without a defect, respectively, and Δn_i and μ_i are the change in the number of atoms and chemical potential of element i, respectively. The chemical potentials of elements Bi (μ_{Bi}) and Te (μ_{Te}) can be written as $\mu_{Bi} = \mu_{Bi}^0 + \Delta\mu_{Bi}$ and $\mu_{Te} = \mu_{Te}^0 + \Delta\mu_{Te}$, where μ_{Bi}^0 and μ_{Te}^0 are the refence chemical potentials of bulk Bi and bulk Te, respectively. Then Equation 1 can be rewritten to Equation 2 as a function of $\Delta\mu_{Te}$, where ΔG^0 is the calculated Gibbs free energy for forming one formula unit of Bi_2Te_3 expressed in Equation 3, with μ_{Bi2Te3} being the chemical potential of one formula unit of Bi_2Te_3. Ribbons with different ZZ or armchair edges are generated with 15-Å separation between the edge and its image and then optimized with an energy cutoff of 400 eV and k-points of 1 × 6×1 and 7 × 1×1 for armchair and ZZ edges, respectively. The formation energy of edges

is calculated using Equation 4, where L is the length of the edge, E^{ribbon} is the total energy of the ribbon, and n_i is the number of atoms of element i. It could be rewritten as a function of $\Delta\mu_{Te}$ in Equation 5.

$$E^f = E^{defect} - E^{pristine} - \sum_i \Delta n_i \, \mu_i \quad \text{(Equation 1)}$$

$$E^f = E^{defect} - E^{pristine} - \sum_i \Delta n_i \, \mu_i{}^0 - \frac{1}{2}\Delta G^0 \Delta n_{Bi} - \left(\Delta n_{Te} - \frac{3}{2}\Delta n_{Bi}\right)\Delta \boldsymbol{\mu}_{Te} \quad \text{(Equation 2)}$$

$$\Delta G^0 = \boldsymbol{\mu}_{Bi_2Te_3} - 2\boldsymbol{\mu}^0_{Bi} - 3\boldsymbol{\mu}^0_{Te} = 2\Delta\boldsymbol{\mu}_{Bi} + 3\Delta\boldsymbol{\mu}_{Te} \quad \text{(Equation 3)}$$

$$E_{edge} = \frac{1}{2L}\left(E^{ribbon} - \sum_i n_i \, \mu_i\right) \quad \text{(Equation 4)}$$

$$E_{edge} = \frac{1}{2L}\left(E^{ribbon} - \frac{1}{2}n_{Bi}\,\boldsymbol{\mu}_{Bi_2Te_3} + \left(\frac{3}{2}n_{Bi} - n_{Te}\right)\left(\boldsymbol{\mu}^0_{Te} + \Delta\boldsymbol{\mu}_{Te}\right)\right) \quad \text{(Equation 5)}$$

RESOURCE AVAILABILITY

Lead contact

Requests for further information and resources should be directed to and will be fulfilled by the lead contact, Dr. Parivash Moradifar (pmoradi@stanford.edu).

Materials availability

The materials generated in this study are available from the corresponding author upon request.

Data and code availability

The data used to support the findings of this study are available from the corresponding authors upon request.

ACKNOWLEDGMENTS

P.M and N.A. acknowledge Penn State MRSEC, Center for Nanoscale Science, under award NSF DMR-1420620, and T.S. acknowledges the Swedish Research Council (awards 2015-06462 and 2015-00520). Additionally, P.M. acknowledges support from the Q-next grant under award DE-AC02-76SF00515. P.A. acknowledges support from the Air Force Office of Scientific Research under award FA9550-18-1-0072. A.C.T.v.D., N.N., and T.W. acknowledge funding from the National Science Foundation 2D Crystal Consortium Materials Innovation Platform (NSF 2DCC-MIP) under cooperative agreement DMR-1539916. Computations for this research were performed on the PSU Institute for Cyber Science Advanced Cyber Infrastructure (ICS-ACI).

AUTHOR CONTRIBUTIONS

P.M. designed the study in consultation with N.A. P.M. carried out the *in situ* TEM experiments and data analysis. T.W., A.C.T.v.D., and N.N. carried out the DFT calculations. T.S. and P.A. carried out the nanoplate synthesis work. The manuscript was drafted by P.M. and edited by all co-authors.

DECLARATION OF INTERESTS

The authors declare no competing interests.

SUPPLEMENTAL INFORMATION

Supplemental information can be found online at https://doi.org/10.1016/j.matt.2024.08.006.

Received: November 1, 2023
Revised: April 16, 2024
Accepted: August 9, 2024
Published: September 9, 2024

REFERENCES

1. Moore, J.E. (2010). The birth of topological insulators. Nature *464*, 194–198.
2. Di Pietro, P., Ortolani, M., Limaj, O., Di Gaspare, A., Giliberti, V., Giorgianni, F., Brahlek, M., Bansal, N., Koirala, N., Oh, S., et al. (2013). Observation of Dirac plasmons in a topological insulator. Nat. Nanotechnol. *8*, 556–560.
3. Ginley, T., Wang, Y., Wang, Z., and Law, S. (2018). Dirac plasmons and beyond: The past, present, and future of plasmonics in 3D topological insulators. MRS Communications *8*, 782–794.
4. Ou, J.Y., So, J.K., Adamo, G., Sulaev, A., Wang, L., and Zheludev, N.I. (2014). Ultraviolet and visible range plasmonics in the topological insulator Bi1.5Sb0.5Te1.8Se1.2. Nat. Commun. 5135–5139.
5. Toudert, J., and Serna, R. (2017). Interband transitions in semi-metals, semiconductors, and topological insulators: a new driving force for plasmonics and nanophotonics. Opt. Mater. Express *7*, 2299–2325.
6. Fei, F., Wei, Z., Wang, Q., Lu, P., Wang, S., Qin, Y., Pan, D., Zhao, B., Wang, X., Sun, J., et al. (2015). Solvothermal synthesis of lateral heterojunction Sb2Te3/Bi2Te3 nanoplates. Nano Lett. *15*, 5905–5911.
7. Wang, Q., Wu, X., Wu, L., and Xiang, Y. (2019). Broadband nonlinear optical response in Bi2Se3-Bi2Te3 heterostructures and its application in all-optical switching. AIP Adv. *9*, 025022.
8. Moradifar, P., Nixon, A.G., Sharifi, T., van Driel, T.B., Ajayan, P., Masiello, D.J., and Alem, N. (2022). Nanoscale mapping and defect-assisted manipulation of surface plasmon resonances in 2D Bi2Te3/Sb2Te3 in-plane heterostructures. Adv. Opt. Mater. *10*, 2101968.
9. Burns, K., Tan, A.M.Z., Gabriel, A., Shao, L., Hennig, R.G., and Aitkaliyeva, A. (2020). Controlling neutral and charged excitons in MoS2 with defects. J. Mater. Res. *35*, 949–957.
10. Zheng, Y.J., Chen, Y., Huang, Y.L., Gogoi, P.K., Li, M.Y., Li, L.J., Trevisanutto, P.E., Wang, Q., Pennycook, S.J., Wee, A.T.S., and Quek, S.Y. (2019). Point defects and localized excitons in 2D WSe2. ACS Nano *13*, 6050–6059.
11. Greben, K., Arora, S., Harats, M.G., and Bolotin, K.I. (2020). Intrinsic and extrinsic defect-related excitons in TMDCs. Nano Lett. *20*, 2544–2550.
12. Park, H.J., Ryu, G.H., and Lee, Z. (2015). Hole defects on two-dimensional materials formed by electron beam irradiation: Toward nanopore devices. Appl. Microsc. *45*, 107–114.
13. Sang, X., Li, X., Zhao, W., Dong, J., Rouleau, C.M., Geohegan, D.B., Ding, F., Xiao, K., and Unocic, R.R. (2018). In-situ edge engineering in two-dimensional transition metal dichalcogenides. Nat. Commun. *9*, 2051.
14. Fan, Y., Robertson, A.W., Zhou, Y., Chen, Q., Zhang, X., Browning, N.D., Zheng, H., Rümmeli, M.H., and Warner, J.H. (2017). Electrical breakdown of suspended mono- and few-layer tungesten disulfide via sulfur depletion identified by in situ atomic imaging. ACS Nano *11*, 9435–9444.
15. Pham, T., Gibb, A.L., Li, Z., Gilbert, S.M., Song, C., Louie, S.G., and Zettl, A. (2016). Formation and dynamics of electron-irradiation-induced defects in hexgonal boron nitride at elevated temperatures. Nano Lett. *16*, 7142–7147.
16. Ryu, G.H., Park, H.J., Ryou, J., Park, J., Hong, S., Lee, Z., Lee, J., Kim, G., Shin, H.S., Bielawski, C.W., and Ruoff, R.S. (2015). Atomic-scale dynamics of triangular hole growth in monolayer hexagonal boron nitride under electron irradiation. Nanoscale *7*, 10600–10605.
17. Cretu, O., Lin, Y.C., and Suenaga, K. (2014). Evidence for active atomic defects in monolayer hexagonal boron nitride: a new mechanism of plasticity in two-dimensional materials. Nano Lett. *14*, 1064–1068.
18. Moradifar, P., Liu, Y., Shi, J., Siukola Thurston, M.L., Utzat, H., van Driel, T.B., Lindenberg, A.M., and Dionne, J.A. (2023). Accelerating qunatum materials development with advances in transmission electron microscopy. Chem. Rev. *123*, 12757–12794.
19. Berlin, K., and Trampert, A. (2018). Phase stability and anisotropic sublimation of cubic Ge-Sb-Te alloy observed by in situ transmission electron microscopy. J. Phys. Chem. C *122*, 2968–2974.
20. Buha, J., Gaspari, R., Del Rio Castillo, A.E., Bonaccorso, F., and Manna, L. (2016). Thermal stability and anisotropic sublimation of two-dimensional colloidal Bi2Te3 and Bi2Se3 nanocrystals. Nano Lett. *16*, 4217–4223.
21. Ohsugi, I.J., Tokunaga, D., Kato, M., Yoneda, S., and Isoda, Y. (2015). Dissociation and sublimation of tellurium from the thermoelectric tellurides. Mater. Res. Innovat. *19*. S5-301.
22. Kang, S.M., Ha, S.S., Jung, W.G., Park, M., Song, H.S., Kim, B.J., and Hong, J.I. (2016). Two-dimensional nanoplates of Bi2Te3 and Bi2Se3 with reduced thermal stability. AIP Adv. *6*, 025110.
23. Shetty, P.P., Kondekar, N., Thenuwara, A.C., Boebinger, M.G., Wright, S.C., Tian, M., and McDowell, M.T. (2020). In situ dynamics during heating of copper intercalated bismuth telluride. Matter *3*, 1246–1262.
24. Shetty, P.P., Wright, S.C., and McDowell, M.T. (2021). Melting, crystallization, and alloying dynamics in nanoscale bismuth telluride. Nano Lett. *21*, 8197–8204.
25. Sharifi, T., Yazdi, S., Costin, G., Apte, A., Coulter, G., Tiwary, C., and Ajayan, P.M. (2018). Impurity-controlled crystal growth in low-dimensional bismuth telluride. Chem. Mater. *30*, 6108–6115.
26. Woehl, T. (2019). Refocusing in situ electron microscopy: moving beyond visualization of nanoparticle self-assembly to gain practical insights into advanced materials characterization. ACS Nano *13*, 12272–12279.
27. Ludwig, T., Guo, L., McCrary, P., Zhang, Z., Gordon, H., Quan, H., Stanton, M., Frazier, R.M., Rogers, R.D., Wang, H.T., and Turner, C.H. (2015). Mechanism of bismuth telluride exfoliation in an ionic liquid solvent. Langmuir *31*, 3644–3652.
28. Zhao, M., Bosman, M., Danesh, M., Zeng, M., Song, P., Darma, Y., Rusydi, A., Lin, H., Qiu, C.W., and Loh, K.P. (2015). Visible surface plasmon modes in single Bi2Te3 nanoplate. Nano Lett. *15*, 8331–8335.
29. Zhang, Y., Hu, L.P., Zhu, T.J., Xie, J., and Zhao, X.B. (2013). High yield Bi2Te3 single crystal nanosheets with uniform morphology via a solvothermal synthesis. Cryst. Growth Des. *13*, 645–651.
30. Hinsche, N.F., Yavorsky, B.Y., Mertig, I., and Zahn, P. (2011). Influence of strain on anisotropic thermoelectric transport in Bi2Te3 and Sb2Te3. Phys. Rev. B *84*, 165214.
31. Narendra, N., and Kim, K.W. (2017). Toward enhanced thermoelectric effects in Bi2Te3/Sb2Te3 heterostructures. Semicond. Sci. Technol. *32*, 035005.
32. Li, H., Liu, H., Zhou, L., Wu, X., Pan, Y., Ji, W., Zheng, B., Zhang, Q., Zhuang, X., Zhu, X., et al. (2018). Strain-tuning atomic substitution in two-dimensional atomic crystals. ACS Nano *12*, 4853–4860.
33. Liang, N., and Zhao, Y. (2023). A review on thermal stability of nanostructured materials. J. Alloys Compd. *938*, 168528.
34. Li, J., Wang, Z., Li, Y., and Deepak, F.L. (2019). In situ atomic-scale observation of kinetic pathways of sublimation in silver nanoparticles. Adv. Sci. *6*, 1802131.
35. Wang, Z.L., Araki, T., Onda, T., and Chen, Z.C. (2018). Effect of annealing on microstructure and thermoelectric properties of hot-extruded Bi-Sb-Te bulk materials. J. Mater. Sci. *53*, 9117–9130.
36. Zhao, L.D., Zhang, B.-P., Liu, W.S., Zhang, H.L., and Li, J.-F. (2009). Effects of annealing on electrical properties of n-type bi2te3 fabricated by mechanical alloying and spark plasma sintering. J. Alloys Compd. *467*, 91–97.
37. Long, B.A., Lau, C.Y., Rodriguez, D.J., Tang, S.A., and Anderson, S.L. (2020). Sublimation kinetics for individual graphite and graphene nanoparticles (NPs): NP-to-NP variations and evolving structure-kinetics and structure-emissivity relationships. J. Am. Chem. Soc. *142*, 14090–14101.
38. Scanlon, D.O., King, P.D.C., Singh, R.P., de la Torre, A., Walker, S.M., Balakrishnan, G., Baumberger, F., and Catlow, C.R.A. (2012). Controlling bulk conductivity in topological insulators: key role of anti-site defects. Adv. Mater. *24*, 2154–2158.
39. Hashibon, A., and Elsässer, C. (2011). First-principles density functional theory study of native point defects in Bi2Te3. Phys. Rev. B *84*, 144117.
40. Vidal, R.C., Zeugner, A., Facio, J.I., Ray, R., Haghighi, M.H., Wolter, A.U., Corredor Bohorquez, L.T., Caglieris, F., Moser, S., Figgemeier, T., et al. (2019). Topological

electronic structure and intrinsic magnetization in MnB4Te7: A Bi2Te3 derivative with a periodic Mn sublattice. Phys. Rev. X *9*, 041065.

41. Garnica, M., Otrokov, M.M., Aguilar, P.C., Klimovskikh, I.I., Estyunin, D., Aliev, Z.S., Amiraslanov, I.R., Abdullayev, N.A., Zverev, V.N., Babanly, M.B., et al. (2022). Nativa point defects and their implications for the dirac point gap at MnBi2Te4 (0001). npj Quantum Mater. *7*.

42. Li, Y., Yang, B., Xu, S., Huang, B., and Duan, W. (2022). Emergent phenomena in magnetic two-dimensional materials and van Der Waals heterostructures. ACS Appl. Electron. Mater. *4*, 3278–3302.

43. Wang, Q.H., Bedoya-Pinto, A., Blei, M., Dismukes, A.H., Hamo, A., Jenkins, S., Koperski, M., Liu, Y., Sun, Q.C., Telford, E.J., et al. (2022). The magnetic genome of two-dimensional van der Waals materials. ACS Nano *16*, 6960–7079.

44. Kohn, W., and Sham, L.J. (1965). Self-consistent equations including exchange and correlation effects. Phys. Rev. *140*, A1133–A1138.

45. Kressea, G., and Furthmüllerb, J. (1966). Efficiency of ab-initio total energy calculations for metals and semiconductors using a plane-wave basis set. Comput. Mater. Sci. *6*, 15–50.

46. Kresse, G., and Furthmüller, J. (1966). Efficient iterative schemes for ab initio total-energy calculations using a plane-wave basis set. Phys. Rev. B *54*, 11169–11186.

47. Blöchl, P.E. (1994). Projector augmented-wave method. Phys. Rev. B *50*, 17953–17979.

48. Perdew, J.P., Burke, K., and Ernzerhof, M. (1996). Generalized Gradient Approximation Made Simple. Phys. Rev. Lett. *77*, 3865–3868.